2008007759

# Modelling of photonic crystal fiber based on layered inclusions

**Thomas Grujic,**[1,*] **Boris T. Kuhlmey,**[1] **C. Martijn de Sterke,**[1] **and Chris G. Poulton**[2]

[1]*Centre for Ultrahigh-bandwidth Devices for Optical Systems (CUDOS), School of Physics A28, University of Sydney, Sydney, NSW 2006, Australia*
[2]*Centre for Ultrahigh-bandwidth Devices for Optical Systems (CUDOS), Department of Mathematical Sciences, University of Technology, Sydney, NSW 2007, Australia*
**Corresponding author: thomas.grujic@gmail.com*

Received May 11, 2009; accepted June 17, 2009;
posted August 10, 2009 (Doc. ID 111163); published September 4, 2009

Photonic crystal fibers often consist of rotationally symmetric inclusions in an otherwise uniform background medium. The band diagrams and modes of such structures can be efficiently calculated using geometry-specific methods that exploit this rotational symmetry. Until now, these have only been applied to fibers in which the inclusions are circular and have a uniform refractive index. Here, we generalize this to arbitrary rotationally symmetric inclusions using a transfer matrix approach, and we implement this approach in an approximate scalar method, which is valid for low-index contrasts and in the rigorous Rayleigh multipole method. We apply the methods to structures incorporating inclusions with graded refractive indices and to structures incorporating metal rings. © 2009 Optical Society of America

*OCIS codes:* 230.4170, 310.5448, 310.6860, 350.2460.

## 1. INTRODUCTION

Photonic crystal fibers (PCFs) are optical fibers composed of a lattice of inclusions in a background matrix surrounding a central core [1]. The majority of PCFs studied consist of a lattice of simple high-index dielectric rods or cylindrical holes around a central core. More recently, however, fibers based on inclusions with a more complicated structure have begun to be investigated involving layered, cylindrically symmetric inclusions as shown schematically in Fig. 1(a). Examples include PCFs based on an array of high-index rings around a central core [2,3] and fibers involving graded index inclusions [4,5]. A metallic coating on the insides of the holes of a PCF opens up the possibility of exploiting very strong surface plasmon resonances with potential applications in sensing and very strong light confinement [3,6,7]. Accurate modelling is required to realize the potential of such fibers.

Existing mode-finding algorithms capable of dealing with fiber structures of arbitrary design include finite-element methods (FEMs) [8] and plane-wave expansion methods (PWEMs) [9]. FEM methods approximate Maxwell's equations by a system of ordinary differential equations and require the PCF profile to be discretized spatially. PWEM methods expand the modal fields in a plane-wave basis to reduce the numerical mode-finding problem to find the eigenvalues of a matrix. This generally requires a large number of plane waves to describe the modes accurately, especially for structures involving high refractive index contrasts. Both methods have the advantage of being applicable to arbitrarily shaped fiber profiles.

There exists also a class of somewhat less general numerical methods for microstructured optical fibers, the so-called integral equation methods [10–14]. These methods are generally more efficient than FEM and PWEM because they assume that the geometry is piecewise homogeneous, but the boundaries between regions are arbitrary.

However, methods tailored toward a specific fiber geometry are more accurate and are usually much faster than generalized methods. In cases with complicated inclusions, the advantages are even more pronounced.

In this paper, we present a set of numerical tools to characterize the properties of PCFs constructed from cylindrically symmetric inclusions with arbitrary radial profiles. A useful approach in studying PCFs is to investigate the properties of their claddings, which in themselves share properties with infinite, periodic lattices as shown in Fig. 1(b) [15]. Light is guided in the core of a fiber if the cladding acts like a mirror—that is, if no modes of the infinite lattice exist. A plot showing for which the combinations of wavelength λ and effective index $n_{\mathrm{eff}}$ modes of the cladding exist (propagation diagram) enables us to predict the spectral transmission of PCFs [16]. We are therefore chiefly concerned with constructing propagation diagrams for infinite lattices of layered inclusions. Here, we are interested in two regimes—one where a scalar treatment of the electromagnetic fields is sufficient, and another that accounts for the fully vectorial nature of both the electric and magnetic fields. We find that in both cases a transfer matrix approach is a streamlined way to track field quantities across boundaries within the inclusion.

Our scalar approach builds on the ideas of Birks *et al.* [17], which allows an investigation of the properties of an infinite periodic system of homogenous dielectric rods of slightly higher refractive index than the background material. We generalize their method to treat a lattice of lay-

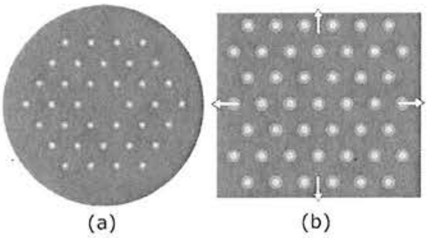

Fig. 1. (Color online) (a) Cross section of an example fiber whose cladding consists of an array of layered inclusions—in this case, dielectric rings representing materials with homogeneous refractive indices. (b) Many of the spectral properties of the fiber follow from those of the associated infinite periodic lattice.

ered inclusions of an arbitrary number of layers with a weak index contrast between all component materials (typically $\Delta n < 1\%$).

To treat the fully vectorial case, we turn to the Rayleigh multipole methods. This class of methods has been particularly useful in modelling PCFs involving arrays of cylindrically symmetric homogeneous rods or holes [18]. Multipole methods enable the calculation of quantities such as the band structure (in the infinite case), projected band diagrams, propagation diagrams, and the photonic density of states [19,20].

These semi-analytic methods expand field quantities in a Fourier–Bessel basis, the natural solutions to the Helmholtz equation in cylindrical coordinates, making them suited to problems with cylindrical symmetries. A far smaller number of terms is then required in the expansion to capture the details of the field relative to a more general algorithm such as a plane-wave method [21]. The general idea behind the method has been adapted to study numerous PCF geometries [19], but not to inclusions with an arbitrary number of layers.

Multipole methods require the scattering matrix of the inclusions, which relates the incoming fields in the vicinity of the inclusion to those scattered from it. The scattering matrix for a homogeneous cylindrical rod or hole is well known and available in analytic closed form [22]. The scattering matrix for an inclusion of uniform refractive index but arbitrary cross section can also be calculated numerically, but at the cost of decreased accuracy and speed [23]. To treat the cases of graded index and coated inclusions using the multipole method, we must calculate the scattering matrix for rotationally symmetric but layered inclusions.

Common to both the derivation of the scattering matrix (for use in the multipole method) and the approximate scalar approach is the need to know the fields in every layer of the inclusion. We use a transfer matrix [24] to link the fields in adjacent layers of the inclusion, an approach that allows us to deal with an arbitrary number of layers.

This paper presents methods to construct propagation diagrams in both the scalar and fully vectorial regimes. Section 2 defines the geometry and coordinate system describing our infinite lattice and gives the general form of the fields in the lattice. Section 3 is a mathematical description of the transfer matrix method we use to find the fields in all layers of the inclusion. Section 4 details our extension of the scalar method developed by Birks *et al.* to the case of layered inclusions. Section 5 uses the transfer matrix formalism to derive the scattering matrix for a layered inclusion. Section 6 compares the propagation diagrams for a photonic crystal composed of graded index inclusions generated by the approximate and fully rigorous multipole methods. Section 7 presents simulations of a PCF consisting of an array of holes coated with a thin metallic layer.

## 2. GEOMETRY AND FIELD REPRESENTATION

We consider the 3D propagation of waves through a periodic array of layered parallel dielectric cylinders. In this paper, we consider only hexagonal lattices, though our approach is valid for other lattice types. The lattice geometry and hexagonal unit cell are shown in Fig. 2. The methods developed here do not apply to the case of interpenetrating inclusions—the outer boundary $r=\rho_N$ must lie entirely within the hexagonal unit cell boundary.

We orient a coordinate system with the $z$ axis parallel to the cylinders and the lattice periodicity in the $x$-$y$ plane. Within a particular unit cell, we look for solutions of the form

$$\mathbf{E}(r,\theta,z,t) = \mathcal{E}(r,\theta)\exp[i(\beta z - \omega t)] + \text{c.c.}\ , \tag{1}$$

$$\mathbf{H}(r,\theta,z,t) = \mathcal{H}(r,\theta)\exp[i(\beta z - \omega t)] + \text{c.c.}, \tag{2}$$

where $\omega$ is the angular frequency related to the free-space wavenumber $k=2\pi/\lambda$ via $\omega=kc$, and $\beta$ is the propagation constant. We also define the effective index as $n_{\text{eff}}=\beta/k$.

All field components satisfy the Helmholtz equation in the homogenous material around the inclusion [25]. Here, we are concerned with two regimes—one that requires a fully vectorial description of both the electric and magnetic field and one where a scalar approach is valid. In the former case, the translational invariance along the $z$ direction means that all field components can be generated from the longitudinal components of the electric and magnetic fields $\mathcal{E}_z$ and $\mathcal{H}_z$ [25]. In the latter, as described in more detail in Section 4, the magnitude of a single transverse component (which we denote by $\Psi$) is sufficient to describe the fields. Using the fact that the fields are nec-

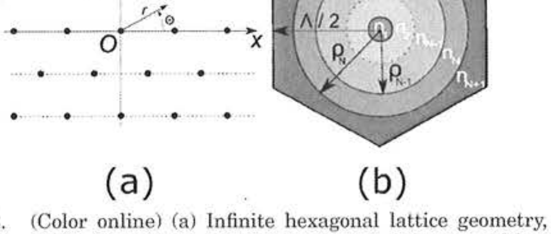

Fig. 2. (Color online) (a) Infinite hexagonal lattice geometry, with coordinate system indicated. (b) Unit cell of hexagonal lattice of layered inclusions of pitch $\Lambda$ representing different component materials. The index of the $p^{\text{th}}$ annulus is $n_p$, with the interface between the $p^{\text{th}}$ and $(p+1)^{\text{th}}$ layers at $\rho_p$.

essarily $2\pi$ periodic in the angular coordinate, it follows that an arbitrary field around the inclusion can be written as a Fourier–Bessel series,

$$\mathcal{V}^p(r,\theta) = \sum_{m=-\infty}^{\infty} (A_m^{\mathcal{V},p} J_m(k_\perp^p r) + B_m^{\mathcal{V},p} H_m^{(1)}(k_\perp^p r))\exp(im\theta), \tag{3}$$

where $\mathcal{V} \in \{\mathcal{E}_z, \mathcal{H}_z, \Psi\}$. $J_m$ denotes the Bessel functions of the first kind of order $m$, and the $H_m^{(1)}$ are the Hankel functions of the first kind of order $m$ [26]. The index $p$ labels the particular layer of the inclusion for which the field expansion is valid, with different expansion coefficients $A_m^{\mathcal{V},p}$, $B_m^{\mathcal{V},p}$ in each layer. The quantity $k_\perp^p$, the transverse wavenumber in each layer, is defined as

$$k_\perp^p = \sqrt{k^2 n_p^2 - \beta^2}. \tag{4}$$

We choose the positive root for the transverse wavenumber outside the inclusion to ensure that fields decay away exponentially in the background medium. The sign of $k_\perp^p$ inside the layered inclusion is immaterial in the cases investigated in this paper, and we choose the positive root to be consistent. A full discussion on the appropriate choice of the sign of $k_\perp^p$ can be found in Appendix A of [27].

Eq. (3) can be broken into two parts—the Bessel functions of the first kind are regular for every argument and correspond to fields with sources exterior to the inclusion, while the Hankel functions diverge at zero and satisfy the outgoing wave equation. Physically, these two terms in the expansion are linked via a scattering of incoming waves from the inclusion, which generates outgoing waves. The major aim of the following sections is to derive a scattering matrix formalism linking the expansion coefficients $B$ associated with sources within the inclusion to those coefficients $A$ associated with fields sourced within the inclusion.

## 3. TRANSFER MATRIX

This section introduces and motivates the transfer matrix formalism we use to relate field expansion coefficients in adjacent layers.

The field components parallel to each boundary between layers must be continuous, as required by Maxwell's equations. In a fully vectorial approach there are four such field components. In the scalar approximation [25], which reduces the fully vectorial fields to a single scalar field, we require the field and its normal derivative to be continuous across each boundary. To solve for the field everywhere in a layered inclusion of $N$ layers for a given azimuthal order $m$ in Eq. (3) then requires solving a $4N \times 4N$ system in the fully vectorial case, or a $2N \times 2N$ system in the scalar approximation.

A more streamlined and versatile method, and one we use in this paper, is to link the fields on either side of an interface via a transfer matrix. More specifically, the fields are expanded in a Bessel function basis, as in Eq. (3). The fields anywhere within a particular layer are controlled by the expansion coefficients of that layer. The cylindrical symmetry of the layered inclusion means that each order $m$ in the expansion of Eq. (3) may be decoupled and treated one at a time. Vectors $\mathbf{v}$ containing the four (in the full vector case) or two (in the scalar case) expansion coefficients for a particular expansion order $m$ in adjacent layers are linked via a $4 \times 4$ or $2 \times 2$ transfer matrix $\mathbf{T}$. Symbolically,

$$\mathbf{v}_{\mathbf{p}\pm 1}^{\mathbf{m}} = \mathbf{T}_{\mathbf{p},\mathbf{p}\pm 1}^{\mathbf{m}} \mathbf{v}_{\mathbf{p}}^{\mathbf{m}}. \tag{5}$$

Importantly, a product of transfer matrices can be used to express the field coefficients in the center of an inclusion with $N$ layers (region 1 in Fig. 2(b)) to those outside the inclusion (region $N+1$):

$$\mathbf{v}_{\mathbf{1}}^{\mathbf{m}} = (\mathbf{T}_{2,1}^{\mathbf{m}} \mathbf{T}_{3,2}^{\mathbf{m}} \ldots \mathbf{T}_{\mathbf{N+1},\mathbf{N}}^{\mathbf{m}}) \mathbf{v}_{\mathbf{N+1}}^{\mathbf{m}}. \tag{6}$$

The physicality of the fields requires the coefficients controlling the diverging part of the fields in the center of the inclusion [the $B_m^{\mathcal{V},1}$ in Eq. (3)] to be zero; otherwise, the field would diverge at the center. In the symbolic notation of this section, specific elements of $\mathbf{v}_{\mathbf{1}}^{\mathbf{m}}$ must be zero. We give examples of the implementation of this condition in two situations described below. Equations (5) and (6), together with the condition that the fields remain finite in the center, allow us to link the fields at any point within the inclusion with those outside it. Importantly for the extension to the multipole method we present in Section 5, the finite field condition additionally implies a connection between the diverging field coefficients $B_m$ and the converging field coefficients $A_m$ outside the inclusion. Our transfer matrix approach is key to both the approximate scalar theory of the next section and the full multipole method of Section 5.

## 4. APPROXIMATE MODEL TO CONSTRUCT PROPAGATION DIAGRAMS

Here we present our extension to the method of Birks *et al.* [17] to generate the edges of photonic bands on a propagation diagram for a low-index contrast structure. The particular approximations and assumptions underlying the method may be found in [17].

A propagation diagram consists of bands of modes of the infinite lattice separated by bandgaps. To construct a propagation diagram, it is only necessary to map out the top (the maximum value of $n_{\text{eff}}$ in a band for a given wavelength) and bottom of the band (minimum value of $n_{\text{eff}}$ in the band for a given wavelength). It is known that the top and bottom of a band correspond to Bloch states with the most bonding and anti-bonding character, respectively. The corresponding boundary conditions at the edge of the unit cell are $\Psi = 0$ and $d\Psi/ds = 0$, respectively, where $s$ is a coordinate normal to the unit cell boundary [17]. These two conditions correspond to particular vectors $\mathbf{v}_{\mathbf{N+1}} \equiv [A_{N+1}, B_{N+1}]^T$,

$$= \left[ -\frac{H_m^{(1)\prime}(k_\perp^{N+1} r_{\text{UC}})}{J'_m(k_\perp^{N+1} r_{\text{UC}})}, 1 \right]^T, \quad \text{for } d\Psi/ds = 0, \tag{7}$$

$$= \left[ -\frac{H_m^{(1)}(k_\perp^{N+1} r_{\text{UC}})}{J_m(k_\perp^{N+1} r_{\text{UC}})}, 1 \right]^T, \quad \text{for } \Psi = 0, \tag{8}$$

where, following Birks *et al.*, we approximate the hexagonal unit cell to a circle with radius $r_{\text{UC}}$ (given in Appendix

A). Comparison with rigorous calculations (which we present in Section 6) validates the approximation in the weak-index contrast limit. This approximation makes it straightforward to impose the boundary conditions on $\Psi$ on the perimeter of the unit cell [17].

Propagation diagrams are constructed by imposing the two boundary conditions corresponding to the top and bottom of a band and enforcing continuity of the scalar field $\Psi$ and its derivative $\mathrm{d}\Psi/\mathrm{d}r$ at each interface between adjacent layers of the inclusion through the application of an appropriate $2\times 2$ transfer matrix $\mathbf{T}^{2\times 2}_{\mathbf{i,i\pm 1}}$, whose form is given explicitly in Appendix A:

$$\begin{bmatrix} A_1 \\ B_1 \end{bmatrix} = \mathbf{T}^{2\times 2}_{2,1}\mathbf{T}^{2\times 2}_{3,2}\ldots\mathbf{T}^{2\times 2}_{\mathbf{N+1,N}}\begin{bmatrix} A_{N+1} \\ B_{N+1} \end{bmatrix}. \tag{9}$$

Equation (9) gives the explicit form of the vector $\mathbf{v}$ in Eq. (6), in the scalar case. Requiring that the fields be finite at the center of the inclusion (in this case, $B_1=0$), allows us to solve for the two effective indices $n_{\text{eff}}=\beta/k$ lying at the top and bottom of a band for a particular wavelength. Varying the wavelength and repeating the procedure maps out the edges of the bands.

Birks *et al.* treated analytically the case of a single solid rod in each circular unit cell. An analogous, purely analytic approach is impossible for the case of an arbitrary number of layers. A transfer matrix approach enables any number of layers to be treated, simply by multiplying the appropriate transfer matrices.

As demonstrated in Section 6, the approximate band-edge finding algorithm works well in the limit of small refractive index contrasts ($\Delta n \approx 1\%$) but breaks down outside this regime. A more general method is required to construct propagation diagrams for periodic lattices of layered inclusions, and to this end we introduce our extension to the Rayleigh multipole method in the next section.

## 5. EXTENSION OF THE RAYLEIGH MULTIPOLE METHOD

In this section, we extend the multipole method to enable modelling of an infinite, perfectly periodic lattice composed of cylindrically symmetric inclusions of arbitrary index profile.

The multipole method involves two essential ingredients [18]—a description of how electromagnetic fields are scattered from an individual inclusion and a description of the structure of the lattice. Our extension to the method then involves only a modification of the formalism describing scattering from a simple cylinder to the case of scattering from a cylindrically symmetric layered inclusion. We therefore do not trace the entire derivation of the multipole method, but show only the derivation of the scattering matrix for a cylindrical inclusion with an arbitrary number of layers.

Armed with our scattering matrix, the multipole method allows us to formulate a condition to determine whether a mode of the infinite lattice exists for a particular combination of wavelength $\lambda$, Bloch vector $\mathbf{k}_0$, and effective index $n_{\text{eff}}$.

### Derivation of the Scattering Matrix

To describe scattering from an inclusion, we must relate the diverging field coefficients $B_m^{\nu}$ of Eq. (3) outside the inclusion (controlling the outgoing waves), to the converging field coefficients $A_m^{\nu}$, also outside the inclusion. In matrix notation, we need to find the scattering matrix $\mathbf{S_m}$, defined by

$$\begin{bmatrix} B_m^{E,N+1} \\ B_m^{H,N+1} \end{bmatrix} = \mathbf{S}_m \begin{bmatrix} A_m^{E,N+1} \\ A_m^{H,N+1} \end{bmatrix}. \tag{10}$$

Scattering from an inclusion depends on the geometry of the inclusion, its refractive index profile, the propagation constant, and the operating wavelength. The derivation of the scattering matrix requires knowledge of the field in all layers of the inclusion, particularly in the center.

As in Eq. (6), we obtain the coefficients in the center of the inclusion in terms of those outside [for a particular order $m$ in the expansion of Eq. (3)] as

$$\begin{bmatrix} A_1^E \\ 0 \\ A_1^H \\ 0 \end{bmatrix} = \mathbf{T}^{4\times 4}_{2,1}\mathbf{T}^{4\times 4}_{3,2}\ldots\mathbf{T}^{4\times 4}_{\mathbf{N+1,N}}\begin{bmatrix} A^E_{N+1} \\ B^E_{N+1} \\ A^H_{N+1} \\ B^H_{N+1} \end{bmatrix} \equiv \mathbf{T}^{4\times 4}\begin{bmatrix} A^E_{N+1} \\ B^E_{N+1} \\ A^H_{N+1} \\ B^H_{N+1} \end{bmatrix}. \tag{11}$$

Here, $\mathbf{T}^{4\times 4}_{\mathbf{i,i+1}}$ is a $4\times 4$ transfer matrix, and Eq. (11) gives the explicit structure of the symbolic vector $\mathbf{v}$ of Eq. (5) in the fully vectorial case. The explicit form of $\mathbf{T}^{4\times 4}_{\mathbf{i,i+1}}$ is given in AppendixB. It links a vector of multipole coefficients on one side of a cylindrical boundary to the corresponding coefficients on the other side for a particular order $m$.

The physicality of the fields requires $B_1^E$, $B_1^H=0$; otherwise, the field would diverge at the center. Equation (11) then yields two equations in only the four multipole coefficients outside the cylinder. These can be solved to give the form of the scattering matrix $\mathbf{S}_m$ defined in Eq. (10). The procedure is illustrated in Appendix B.

Knowledge of the scattering matrix for layered inclusions is then sufficient to use the existing multipole formalism to find the modes of finite or infinite arrays of layered inclusions. A change of basis operator $\mathbf{K}$ is used to express the fields scattered from all other inclusions in the local coordinates of a particular inclusion in the lattice. Conservation of the total ingoing and outgoing fields in the vicinity of the inclusion then allows a self-consistent matrix equation to be written for the field expansion coefficients [18].

Symbolically, a mode of the system exists when

$$[\mathbf{I}-\mathbf{SK}]\mathbf{B} \equiv \mathbf{P}(\lambda,\mathbf{k}_0,n_{\text{eff}})\mathbf{B}=0. \tag{12}$$

Here, $\mathbf{S}$ is a scattering matrix combining the $\mathbf{S_m}$ for all orders $m$. $\mathbf{K}$ contains lattice sums describing the structure of the lattice in the case of an infinite periodic lattice [28,29]. $\mathbf{B}$ is a vector holding the diverging field coefficients of all orders for a single unit cell (in the infinite case), or for all inclusions (in the finite PCF case). A propagation diagram for an infinite lattice can be constructed by scanning the Bloch vector $\mathbf{k}_0$ over the irreducible Brillouin zone perimeter for a given effective $(\lambda,n_{\text{eff}})$

combination [30]. The existence of a mode corresponds to the determinant of **P** being zero.

## 6. NUMERICAL SIMULATIONS

In this section, we compare the performance of the approximate band-finding theory of Section 4 with that of the fully vectorial multipole method of Section 5. The structure we consider is a hexagonal array of pitch $\Lambda = 6.7\ \mu\text{m}$ made up of graded index cylinders in a silica background. The characteristics of the inclusions match those of a fiber whose spectral properties were investigated numerically and experimentally by Kuhlmey *et al.* [5]. In that work, differences between theoretical and experimental results were in part attributed to the inability to accommodate both the material dispersion and an accurate description of the index profile of the cylinders in numerical simulations. The methods developed in this paper allow us to evaluate this claim. Each cylinder has a graded refractive index distribution above that of the background silica, given by

$$n(r) = \begin{cases} n_{\text{silica}}(1 + \Delta n_{\text{GI}}(1 - (r/r_0)^{\alpha})), & \text{if } r < 0 \\ n_{\text{silica}}, & \text{if } r \geq r_0 \end{cases}, \quad (13)$$

where $r$ is the distance from the cylinder's center, $\alpha \approx 4.7$, $\Delta n_{\text{GI}} \approx 0.0203$, $r_0 = 1.5927$, and $n_{\text{silica}}$ is the wavelength-dependent index of fused silica, obtained using a Sellmeier expansion. This refractive index profile is the black dashed curve in Fig. 3.

To generate propagation diagrams for this structure, we discretize the graded index profile, as illustrated by the step index function in Fig. 3. This is done by dividing the inclusion into $N$ concentric layers of equal refractive index steps $\Delta n$, whose radii $\bar{r}_i$ are calculated by taking the square root of the average of the square of the radial coordinate $r$ weighted by the index distribution over each index step:

$$\bar{r}_i = \sqrt{\frac{1}{\Delta n}\int_{n_i}^{n_{i+1}} r^2(n)\mathrm{d}n}. \quad (14)$$

Here, $n_i$ and $n_{i+1}$ are the refractive indices on the edges of each index step. Such an area-weighted discretization ensures there are more steps approximating the graded profile where it varies most rapidly with $r$, while also taking into account the cylindrical geometry of the inclusion.

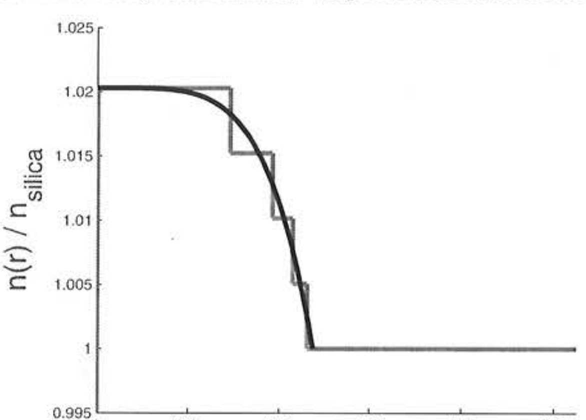

Fig. 3. (Color online) Graded index profile of each cylinder in the hexagonal infinite lattice (black curve) with an example discretization into four layers.

### A. Approximate Band Edges

To obtain accurate band edges using the approximate theory of Section 4, we must use an adequately large number of approximating layers $N$. To establish criteria for constructing accurate propagation diagrams, we calculate band edges for a number of different approximating layers, as in Fig. 4.

The wavelength range we use corresponds to that investigated by Kuhlmey *et al.* Each band in the propagation diagram corresponds to a particular $m$ in the field expansion of Eq. (3) and therefore consists of modes with a particular azimuthal field dependence.

We see that simply approximating the graded index profile by a single rod ($N=1$) or even a double-step index distribution ($N=2$) is not sufficient to capture accurately all details of the band structure. The band edges for $N=8$ and $N=10$ overlap to within the thickness of the lines used to plot them. Subsequent graded index inclusion simulations therefore used $N=8$ approximating layers. The dotted curves in Fig. 5, to be discussed below, are the $N=8$ band edges generated by the approximate method.

### B. Full Multipole Propagation Diagrams

We now use the fully vectorial multipole formalism of Section 5 to construct rigorous band diagrams for our structure of interest. The scattering matrix $\mathbf{S}_m$ in Eq. (10) is calculated using eight approximating layers, and field quantities were expanded in eleven terms (corresponding to $m$ ranging from −5 to 5).

The solid black regions of Fig. 5 show where modes of the infinite lattice exist, as found by the multipole method. The white regions between the black photonic bands show where the bandgaps lie in $n_{\text{eff}} - \lambda$ space. The curves show the results of a commercial plane-wave numerical package. The density of these lines gives some limited information on the density of photonic states. We note that our formulation can also calculate detailed density of states data, though we are here only interested in

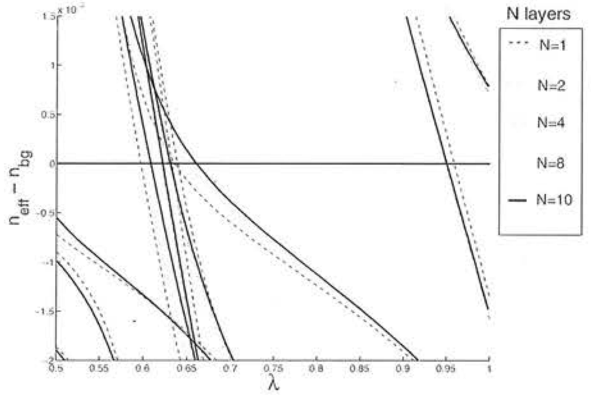

Fig. 4. (Color online) Band edges for an infinite lattice of graded inclusions, generated by the scalar method of Section 4, for different numbers of approximating discretized layers $N$. Here $n_{\text{bg}}$ is the wavelength dependent background index of silica, obtained using a Sellmeier expansion [31].

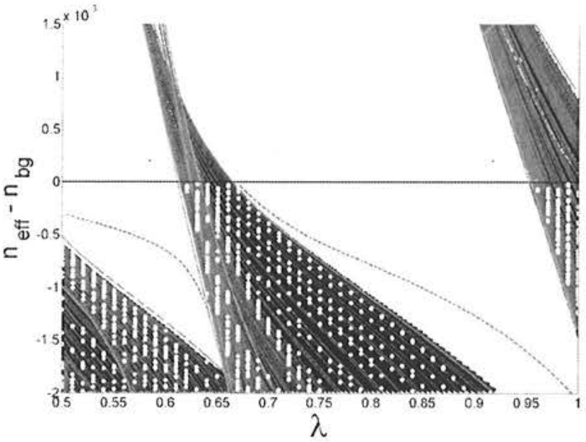

Fig. 5. (Color online) Comparison of approximate band-edge finding algorithm (curves) with fully vectorial multipole method (black solid regions). Also shown are the results of a commercial plane-wave package (lines). White dots are the cladding modes of a finite fiber consisting of three layers of graded inclusions around a central missing inclusion. Gray dashed curves are core modes for this finite fiber.

the combinations of effective index and wavelength for which a bandgap exists (i.e., when the structure supports no modes).

The two photonic bandgaps beneath the light line $n_{\mathrm{eff}}=n_{\mathrm{bg}}$ between bands can be used to guide a core mode in a finite photonic crystal fiber. The gray dashed curves in Fig. 5 are core modes calculated for a fiber consisting of three rings of graded inclusions around a central solid core that were formed by removing an inclusion. The white dots are the cladding modes of the same fiber and coincide almost exactly with the photonic bands of the infinite unperturbed lattice.

While these results, which take into account both the actual nature of the graded index inclusion profile and the dispersion of silica, differ appreciably from the numerical results previously obtained by Kuhlmey *et al.* [5], the agreement with experimental results is not improved. The discrepancy may be due to other factors, such as an inaccurate characterization of the experimental fiber's properties, in particular the exact index profile of each inclusion, and the pitch of the acoustic grating used.

Figure 5 shows that the approximate theory gives very good agreement with the full multipole simulations, as expected in this limit of a weak index contrast between the maximum index of the inclusion and the background index of silica. In weak contrast situations where only the positions of the bands and bandgaps are required, it is much faster to use the approximate approach than a fully vectorial method.

However, the assumption that the electromagnetic fields can be treated as scalar quantities breaks down in systems with a higher contrast between the permittivities of the component materials, rendering the approximate method inaccurate. The multipole formalism deals well with inclusions consisting of concentric layers with high refractive index contrasts between them, as it does not suffer from convergence issues inherent in other approaches such as the plane-wave class of methods.

## 7. ANALYSIS OF THIN METAL COATINGS

An example of a situation involving a very high contrast in the permittivity of component materials is that of a lattice of air-filled thin metallic rings in a silica background. Photonic crystal fibers involving metals open up the possibility of exploiting surface plasmon polariton resonances, with potential applications in sensing and optoelectronic components [32].

We simulate structures similar to those studied both experimentally by Schmidt *et al.* [33] and numerically by Poulton *et al.* [6] , who studied the properties of an infinite hexagonal lattice of solid metallic nanowires. We instead model lattices of air-filled thin metal rings of varying thicknesses in a silica background. Following Poulton *et al.*, we take the permittivity of the rings $\varepsilon_m=-125.3$ to be that of silver at the vacuum wavelength 1.55 $\mu$m and construct propagation diagrams by varying the scale of the structure rather than the wavelength. Additionally, we neglect material absorption ($\mathrm{Im}[\varepsilon_m]=0$). The extension of our method to the case of a structure involving materials with a finite imaginary component to their permittivities is straightforward but beyond the scope of this paper, as discussed in the conclusion. The permittivity of the background silica at this wavelength is $\varepsilon_s=2.085$. We fix the outer ring radius at $b=0.15\Lambda$ and vary the inner radius $a$.

The photonic bands and bandgaps for a number of different ring thicknesses are shown in Fig. 6 in terms of normalized frequency and the quantity $(n_{\mathrm{eff}}-n_{\mathrm{bg}})k_0\Lambda \equiv (\beta-n_{\mathrm{bg}}k_0)\Lambda$. The white regions indicate where modes of the infinite lattice exist, and the gray areas in between are the photonic bandgaps. We remark that propagation diagrams are not appreciably different from those for the corresponding lattice of solid metal rods until the ring thickness becomes comparable to the skin depth of the metal. All three propagation diagrams in Fig. 6 correspond to such a regime in which the ringlike nature of the inclusions is important.

Bound modes of single thin metallic rings in a silica background are also plotted as dots in Fig. 6 and are cut off at $n_{\mathrm{eff}}=n_{\mathrm{background}}$. For an infinite periodic lattice, the plasmonic modes of the individual rings couple together, broaden into the white bands, and extend below the cutoff [34].

Figure 6(a) indicates the azimuthal order $m$ of the modes of the isolated rings that broaden into the three bands visible for $n_{\mathrm{eff}}>n_{\mathrm{background}}$. Between ring radius ratios $a/b=0.95$ and 0.98, we see a transition in the behavior of the $m=1$ band of modes. For $a/b=0.95$, the $m=1$ mode of the isolated metal ring broadens into a photonic band near $k_0\Lambda=0$, while for $a/b=0.98$ a bandgap has opened up at low frequencies. Figure 6(b) shows the intermediate behavior.

We can explain this transition by realizing that in the low-frequency limit, the wavelength is much greater than the overall size of individual inclusions. The details of the rings cannot be resolved by the fields, and we may treat the inclusions as a uniform material with a homogenized permittivity. Below a critical ring thickness, the homogenized permittivity of the inclusions passes from negative to positive. Plasmonic modes can only exist when there is a difference in sign between the permittivities of adjacent

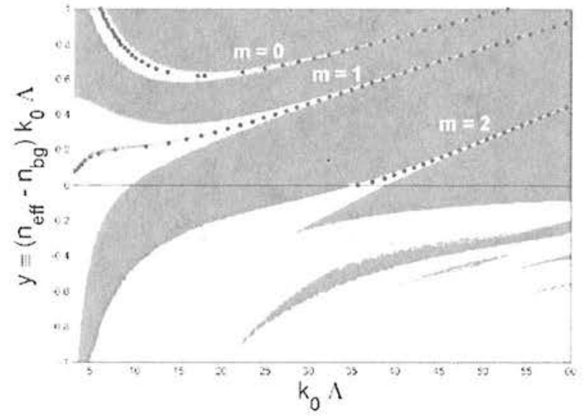

(a) a / b = 0.95

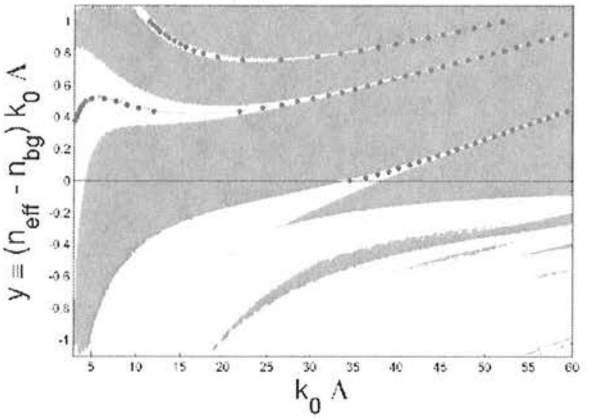

(b) a / b = 0.965

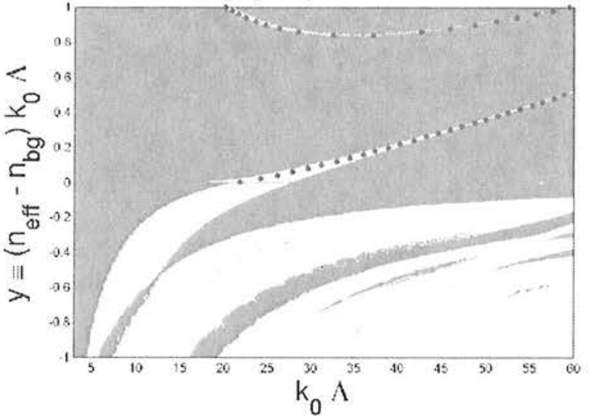

(c) a / b = 0.98

Fig. 6. (Color online) Propagation diagrams for infinite hexagonal lattices, pitch $\Lambda = 1$ $\mu$m, of metallic rings of varying thicknesses. Dots indicate the bound modes of single metallic rings in a silica background, which exist for $n_{\mathrm{eff}} > n_{\mathrm{bg}}$. Metal permittivity is $\varepsilon_m = -125.4$ and background permittivity is 2.085.

materials, and so the bandgap apparent in Fig. 6(c) at low frequencies opens up below this critical ring thickness.

In the high-frequency limit, the dispersion curves of the rings approach those of equivalent thin metallic slabs whose widths are equal to the relevant ring thickness, bounded by air on one side and silica on the other.

## 8. DISCUSSION AND CONCLUSION

The methods presented in this paper allow fast, accurate calculation of the properties of photonic crystal fiber based on cylindrically symmetric layered inclusions. The approximate method of Section 4 allows us to map out the photonic band edges on a propagation diagram for infinite, periodic structures with weak refractive index contrasts. Within the domain of applicability, the advantages in using this method over the computationally intensive multipole method to generate band edge information rapidly are marked, requiring minutes (rather than hours) to locate the positions of the bands. It is then possible to rapidly predict the wavelength ranges where core modes of a finite layered PCF exist.

The ability to discretize an inclusion with a radially dependent refractive index profile into an arbitrary number of layers, as in the case of the smoothly varying graded index cylinders of Section 6, allows us to treat PCFs composed of such inclusions accurately.

For fibers with a higher permittivity contrast, the vectorial nature of the electromagnetic fields can no longer be ignored. The scattering matrix derived in Section 5 allows efficient, accurate generation of propagation diagrams and calculation of core mode dispersion in the case of finite PCF.

In common with existing multipole algorithms that solve simple circular inclusion problems, the circular symmetry of the inclusions is built in, making a multipole approach to the simulation of layered inclusion PCF very efficient and accurate when compared with algorithms capable of simulating more general index profiles. The efficiency becomes further pronounced as more layers are added, as the element of the multipole method that requires the most computational resources is the evaluation of lattice sums, with the scattering matrix calculation requiring far less computing power. Coupled with the fact that high permittivity contrasts between layers present no additional numerical convergence issues, this makes our multipole formulation particularly well suited to modelling PCFs composed of cylindrically symmetric inclusions.

The numerical analysis of PCF involving thin metallic coatings in Section 7 required the same number of terms in the field expansions as did the modelling of the all-dielectric graded index fiber of Section 6. The extremely large permittivity contrasts present in metal–dielectric structures present appreciable convergence difficulties in more general approaches, such as the plane-wave expansion method [22].

Though we have here studied only the case of lossless metals (i.e., metals with purely real permittivities) at one operating wavelength, the multipole formalism easily accommodates more general dispersive materials with complex permittivities. The effects of material dispersion are included easily as the multipole algorithm searches for modes at a fixed frequency, which is then varied across the simulation window. To include the effects of loss, the mode-finding algorithm, which involves finding the roots of the determinant of the matrix **P** in Eq. (12), must be extended in this case to search over complex values of the modal effective index rather than just purely real ones.

We also note that while the multipole results presented in this paper give only a binary indication of whether or not one or more modes exist at a given point in a propagation diagram, density of states information can be generated by counting the number of times Eq. (12) is satisfied while tracing around the perimeter of the irreducible Brillouin zone.

## APPENDIX A

This appendix presents a transfer matrix method to map out the band edges on a propagation diagram for an infinite lattice of layered dielectric inclusions in the limit of a weak refractive index contrast. The assumption of a circular unit cell with radius $r_{\mathrm{UC}}=(\sqrt{3}/2\pi)^{1/2}\Lambda$ (this choice preserves the filling fraction) is identical to that of Birks *et al.* [17].

The scalar field $\Psi$ has the form given in Eq. (3). We isolate one particular order $m=l$ in the expansion for the field in region $p$ (different $m$ yield modes with different azimuthal dependence):

$$\psi^p=[A_l^pJ_l(k_\perp^p r)+B_l^pH_l(k_\perp^p r)]\exp(il\theta). \tag{A1}$$

Requiring that both $\psi$ and $d\psi/dr$ be continuous across an interface at radial coordinate $r=\rho_p$, we can link the vector of field coefficients $[A^pB^p]^T$ on one side of the interface to those on the other $[A^{p+1}B^{p+1}]^T$ via a $2\times2$ transfer matrix $\mathbf{T}_{\mathbf{i,i+1}}^{\mathbf{2\times2}}$:

$$\mathbf{T}_{\mathbf{i,i+1}}^{\mathbf{2\times2}}=\frac{1}{k_\perp^{i+1}[J_l(y)H_l^{(1)'}(y)-J_l'(y)H_l^{(1)}(y)]}\begin{pmatrix} k_\perp^{i+1}H_l^{(1)'}(y)J_l(x)-k_\perp^iH_l^{(1)}(y)J_l'(x) & k_\perp^{i+1}H_l^{(1)'}(y)H_l^{(1)}(x)-k_\perp^iH_l^{(1)}(y)H_l^{(1)'}(x)\\ k_\perp^iJ_l(y)J_l'(x)-k_\perp^{i+1}J_l(x)J_l'(y) & k_\perp^iJ_l(y)H_l^{(1)'}(x)-k_\perp^{i+1}H_l^{(1)}J_l'(y)\end{pmatrix}, \tag{A2}$$

where $x=k_\perp^p\rho_p$ and $y=k_\perp^{p+1}\rho_p$. To find the photonic band edges, we implement the boundary conditions discussed in Section 4 on the edge of our circular unit cell. For instance, the top of the band corresponds to a zero derivative $d\Psi/dr$ at $r=r_{UC}$, which corresponds to the particular choice $[A^{N+1}B^{N+1}]^T=[-H_l^{(1)'}(k_\perp^{N+1})/J_l'(k_\perp^{N+1})1]^T$. The transfer matrix is then used to repeatedly step across dielectric interfaces, as in Eq. (9).

## APPENDIX B

We derive here the explicit form of the $4\times4$ transfer matrix $\mathbf{T}_{\mathbf{i,i+1}}^{\mathbf{4\times4}}$ defined in Eq. (11). Our approach is similar to that of Yeh and Yariv [24], though we use a basis of Bessel functions of the first kind and Hankel functions of the first kind, while Yeh and Yariv used a basis with Bessel functions of the second kind in place of Hankel functions.

The field components tangential to a cylindrical interface between layers in an inclusion (the $z$ and $\theta$ components) must be continuous. The multipole expansion coefficients $A_m^{\mathcal{V}}$, $B_m^{\mathcal{V}}$ generate the longitudinal components $\mathcal{V}_z$ of the electromagnetic fields, and we can generate the azimuthal components from the longitudinal components using Maxwell's equations as

$$\mathcal{E}_\theta=\frac{i\beta}{k^2n_p^2-\beta^2}\left(\frac{\partial}{r\partial\theta}\mathcal{E}_z-\frac{\omega}{\beta}\frac{\partial}{\partial r}\mathcal{H}_z\right), \tag{B1}$$

$$\mathcal{H}_\theta=\frac{i\beta}{k^2n_p^2-\beta^2}\left(\frac{\partial}{r\partial\theta}\mathcal{H}_z+\frac{\omega}{\beta}\frac{\partial}{\partial r}\mathcal{E}_z\right). \tag{B2}$$

This allows us to write continuity relations for the four tangential field components across an interface in terms of the multipole expansion coeffcients $A_m^{\mathcal{V}}$, $B_m^{\mathcal{V}}$.

The continuity of the longitudinal component of the electric field $\mathcal{E}_z$ across a boundary between regions $i$ and $i+1$ at radial coordinate $r=\rho$ is then written:

$$A_p^EJ_m(k_{\perp,i}\rho)+B_p^EH_m(k_{\perp,i}\rho)=A_{i+1}^EJ_m(k_{\perp,i+1}\rho)+B_{i+1}^EH_m(k_{\perp,i+1}\rho). \tag{B3}$$

Similarly, continuity of $\mathcal{E}_\theta$ gives the following relation:

$$\frac{1}{(k_\perp^p)^2}\left(\frac{im}{\rho}[A_p^EJ_m(k^p\rho)+B_p^EH_m(k^p\rho)]-\frac{\omega k_\perp^p}{\beta}[A_p^HJ_m'(k_\perp^p\rho)+B_p^HH_m'(k_\perp^p\rho)]\right), \tag{B4}$$

$$=\frac{1}{(k_\perp^{i+1})^2}\left(\frac{im}{\rho}[A_2^EJ_m(k_\perp^{i+1}\rho)+B_2^EH_m(k_\perp^{i+1}\rho)]-\frac{\omega k_\perp^{i+1}}{\beta}[A_2^HJ_m'(k_\perp^{i+1}\rho)+B_2^HH_m'(k_\perp^{i+1}\rho)]\right). \tag{B5}$$

Similar relations hold for the longitudinal and azimuthal components of the magnetic field. The four resulting equations can then be written in the matrix form

$$\mathbf{M}(i,\rho)\begin{bmatrix}A_p^E\\B_p^E\\A_p^H\\B_p^H\end{bmatrix}=\mathbf{M}(i+1,\rho)\begin{bmatrix}A_{i+1}^E\\B_{i+1}^E\\A_{i+1}^H\\B_{i+1}^H\end{bmatrix}. \tag{B6}$$

Finally then, the transfer matrix can be found as $\mathbf{T}_{\mathbf{i,i+1}}^{\mathbf{4\times4}}=\mathbf{M}^{-1}(i+1,\rho)\mathbf{M}(i,\rho)$. Explicitly, defining $x=k_\perp^p\rho$ and $y=k_\perp^{i+1}\rho$ and writing $\mathbf{T}_{\mathbf{i,i+1}}^{\mathbf{4\times4}}$ as

$$\mathbf{T}^{4\times 4}_{\mathbf{i,i+1}} = \frac{\pi y}{2}\begin{pmatrix} t_{11} & t_{12} & t_{13} & t_{14} \\ t_{21} & t_{22} & t_{23} & t_{24} \\ t_{31} & t_{32} & t_{33} & t_{34} \\ t_{41} & t_{42} & t_{43} & t_{44} \end{pmatrix}, \qquad \text{(B7)}$$

we obtain the elements as

$$t_{11} = J_l(x)H_l^{(1)'}(y) - (k_\perp^{i+1}\varepsilon_p/k_\perp^p\varepsilon_{i+1})J_l'(x)H_l^{(1)}(y),$$

$$t_{12} = H_l^{(1)}(x)H_l^{(1)'}(y) - (k_\perp^{i+1}\varepsilon_p/k_\perp^p\varepsilon_{i+1})H_l^{(1)'}(x)H^{(1)}(y),$$

$$t_{13} = (i\beta l/\omega\varepsilon_{i+1})(1/y - k_\perp^{i+1}/(xk_\perp^p))J_l(x)H_l^{(1)}(y),$$

$$t_{14} = (i\beta l/\omega\varepsilon_{i+1})(1/y - k_\perp^{i+1}/(xk_\perp^p))H_l^{(1)}(x)H_l^{(1)}(y),$$

$$t_{21} = (k_\perp^{i+1}\varepsilon_p/k_\perp^p\varepsilon_{i+1})J_l'(x)J_l(y) - J_l(x)J_l'(y),$$

$$t_{22} = H_l^{(1)}(x)H_l^{(1)'}(y) - (k_\perp^{i+1}\varepsilon_p/k_\perp^p\varepsilon_{i+1})H_l^{(1)'}(x)H^{(1)}(y),$$

$$t_{23} = (i\beta l/\omega\varepsilon_{i+1})(1/y - k_\perp^{i+1}/(xk_\perp^p))J_l(x)H_l^{(1)}(y),$$

$$t_{24} = (i\beta l/\omega\varepsilon_{i+1})(1/y - k_\perp^{i+1}/(xk_\perp^p))H_l^{(1)}(x)H_l^{(1)}(y),$$

$$t_{31} = (i\beta l/\omega)(k_\perp^{i+1}/(xk_\perp^p) - 1/y)J_l(x)H_l^{(1)}(y),$$

$$t_{32} = (i\beta l/\omega)(k_\perp^{i+1}/(xk_\perp^p) - 1/y)H_l^{(1)}(x)H_l^{(1)}(y),$$

$$t_{33} = J_l(x)H_l^{(1)'}(y) - (k_\perp^{i+1}/k_\perp^p)J_l'(x)H_l^{(1)}(y),$$

$$t_{34} = H^{(1)}(x)H_l^{(1)'}(y) - (k_\perp^{i+1}/k_\perp^p)H^{(1)'}(x)H_l^{(1)}(y),$$

$$t_{41} = (i\beta l/\omega)(1/y - k_\perp^{i+1}/(xk_\perp^p))J_l(x)J_l(y),$$

$$t_{42} = (i\beta l/\omega)(1/y - k_\perp^{i+1}/(xk_\perp^p))H_l^{(1)}(x)J_l(y),$$

$$t_{43} = (k_\perp^{i+1}/k_\perp^p)J_l'(x)J_l(y) - J_l(x)J_l'(y),$$

$$t_{44} = (k_\perp^{i+1}/k_\perp^p)H_l^{(1)'}(x)J_l(y) - H_l^{(1)}(x)J_l'(y).$$

We now show how the scattering matrix $\mathbf{S_m}$ is obtained from Eq. (11). Writing the elements of $\mathbf{T}^{4\times 4}$ as $T_{ij}$, we can expand the matrix equation of Eq. (11) to obtain

$$T_{21}A_{N+1}^E + T_{22}B_{N+1}^E + T_{23}A_{N+1}^H + T_{24}B_{N+1}^H = 0, \qquad \text{(B8)}$$

$$T_{41}A_{N+1}^E + T_{42}B_{N+1}^E + T_{43}A_{N+1}^H + T_{44}B_{N+1}^H = 0. \qquad \text{(B9)}$$

These equations only involve field expansion coefficients outside the inclusion and can be solved for the diverging field coefficients in terms of the converging coefficients as

$$\begin{bmatrix} B^E \\ B^H \end{bmatrix} = \frac{1}{\Delta}\begin{bmatrix} T_{24}T_{41} - T_{44}T_{21} & T_{24}T_{43} - T_{44}T_{23} \\ T_{42}T_{21} - T_{22}T_{41} & T_{42}T_{23} - T_{22}T_{43} \end{bmatrix}\begin{bmatrix} A^E \\ A^H \end{bmatrix} \equiv \mathbf{S_m}\begin{bmatrix} A^E \\ A^H \end{bmatrix}, \qquad \text{(B10)}$$

where $\Delta = T_{22}T_{44} - T_{42}T_{24}$.

## ACKNOWLEDGMENTS

This research was supported under the Australian Research Council's (ARC) Discovery Project and Centre of Excellence funding schemes. CUDOS is an ARC Centre of Excellence.

## REFERENCES

1. J. C. Knight, "Photonic crystal fibers," Nature **424**, 847–851 (2003).
2. J. M. Stone, G. J. Pearce, F. Luan, T. A. Birks, J. C. Knight, A. K. George, and D. M. Bird, "An improved photonic bandgap fiber based on an array of rings," Opt. Express **14**, 6291–6296 (2006).
3. B. T. Kuhlmey, K. Pathmanandavel, and R. C. McPhedran, "Multipole analysis of photonic crystal fibers with coated inclusions," Opt. Express **14**, 10851–10864 (2006).
4. T. A. Birks, F. Luan, G. J. Pearce, A. Wang, J. C. Knight, and D. M. Bird, "Bend loss in all-solid bandgap fibers," Opt. Express **14**, 5688–5698 (2006).
5. B. T. Kuhlmey, F. Luan, L. Fu, D. I. Yeom, B. J. Eggleton, A. Wang, and J. Knight, "Experimental reconstruction of bands in solid core photonic bandgap fibers using acoustic gratings," Opt. Express **16**, 13845–13856 (2008).
6. C. G. Poulton, M. A. Schmidt, G. J. Pearce, G. Kakarantzas, and P. S. J. Russell, "Numerical study of guided modes in arrays of metallic nanowires," Opt. Lett. **32**, 1647–1649 (2007).
7. J. Hou, D. Bird, A. George, S. Maier, B. Kuhlmey, and J. C. Knight, "Metallic mode confinement in microstructured fibers," Opt. Express **16**, 5983–5990 (2008).
8. C. T. Chan, Q. L.Yu, and K. M. Ho, "Order-N spectral method for electromagnetic waves," Phys. Rev. B **51**, 16635–16642 (1995).
9. K. M. Leung and Y. F. Liu, "Full vector wave calculation of photonic band structures in face-centered-cubic dielectric media," Phys. Rev. Lett. **65**, 2646–2649 (1990).
10. N. Guan, S. Habu, K. Takenaga, K. Himeno, and A. Wada, "Boundary element method for analysis of holey optical fibers," J. Lightwave Technol. **21**, 1787–1792 (2003).
11. T. L. Wu and C. H. Chao, "Photonic crystal fiber analysis through the vector boundary-element method: effect of elliptical air hole," IEEE Photon. Technol. Lett. **16**, 126–128 (2004).
12. H. Cheng, W. Crutchfield, M. Doery, and L. Greengard, "Fast, accurate integral equation methods for the analysis of photonic crystal fibers. I: Theory," Opt. Express **12**, 3791–3805 (2004).
13. E. Pone, A. Hassani, S. Lacroix, A. Kabashin, and M. Skorobogatiy, "Boundary integral method for the challenging problems in bandgap guiding, plasmonics, and sensing," Opt. Express **15**, 10231–10246 (2007).
14. A. Hochman and Y. Leviatan, "Efficient and spurious-free integral-equation-based optical waveguide mode solver," Opt. Express **15**, 14431–14453 (2007).
15. T. A. Birks, J. C. Knight, and P. S. J. Russell, "Endlessly single-mode photonic crystal fiber," Opt. Lett. **22**, 961–963 (1997).
16. P. S. J. Russell, T. A. Birks, J. C. Knight, and B. J. Mangan, "Photonic crystal fibers," US Patent 6,990,282 (2006).
17. T. A. Birks, G. J. Pearce, and D. D. M. Bird, "Approximate band structure calculation for photonic bandgap fibers," Opt. Express **14**, 9483–9490 (2006).
18. L. C. Botten, R. C. McPhedran, C. M. de Sterke, N. A. Nicorovici, A. A. Asatryan, G. H. Smith, T. N. Langtry, T. P. White, D. P. Fussell, and B. T. Kuhlmey, *From Multipole Methods to Photonic Crystal Device Modelling* (CRC Press, 2005).

19. L. C. Botten, R. C. McPhedran, N. A. Nicorovici, A. A. Asatryan, C. M. de Sterke, P. A. Robinson, K. Busch, G. H. Smith, and T. N. Langtry, "Rayleigh multipole methods for photonic crystal calculations," PIER **41**, 21–60 (2003), doi:10.2528/PIER02010802.
20. R. C. McPhedran, L. C. Botten, J. McOrist, A. A. Asatryan, C. M. de Sterke, and N. A. Nicorovici, "Density of states functions for photonic crystals," Phys. Rev. E **69**, 016609 (2004).
21. B. T. Kuhlmey, T. P. White, G. Renversez, D. Maystre, L. C. Botten, C. M. de Sterke, and R. C. McPhedran, "Multipole method for microstructured optical fibers. II. Implementation and results," J. Opt. Soc. Am. B **19**, 2331–2340 (2002).
22. T. P. White, B. T. Kuhlmey, R. C. McPhedran, D. Maystre, G. Renversez, C. M. de Sterke, and L. C. Botten, "Multipole method for microstructured optical fibers. I. Formulation," J. Opt. Soc. Am. B **19**, 2322–2330 (2002).
23. S. Campbell, R. C. McPhedran, C. M. de Sterke, and L. C. Botten, "Differential multipole method for microstructured optical fibers," J. Opt. Soc. Am. B **21**, 1919–1928 (2004).
24. P. Yeh, A. Yariv, and E. Marom, "Theory of Bragg fiber," J. Opt. Soc. Am. **68**, 1196–1201 (1978).
25. A. W. Snyder and J. D. Love, *Optical Waveguide Theory* (Academic, 1983).
26. M. Abramowitz and I. A. Stegun, *Handbook of Mathematical Functions with Formulas, Graphs, and Mathematical Tables* (Dover, 1964), ninth Dover printing, tenth GPO printing ed.
27. B. Kuhlmey, "Theoretical and numerical investigation of the physics of microstructured optical fibers," Ph.D. thesis, University of Sydney and Université Aix-Marseille III (2006). http://setis.library.usyd.edu.au/adt/public html/adt-NU/public/adt-NU20040715.171105/.
28. R. C. McPhedran, N. A. Nicorovici, L. C. Botten, and K. A. Grubits, "Lattice sums for gratings and arrays," J. Math. Phys. **41**, 7808–7816 (2000).
29. S. K. Chin, N. A. Nicorovici, and R. C. McPhedran, "Green's function and lattice sums for electromagnetic scattering by a square array of cylinders," Phys. Rev. E **49**, 4590–4602 (1994).
30. T. P. White, R. C. McPhedran, L. C. Botten, G. Smith, and C. M. de Sterke, "Calculations of air-guided modes in photonic crystal fibers using the multipole method," Opt. Express **9**, 721–732 (2001).
31. G. P. Agrawal and R. W. Boyd, *Nonlinear Fiber Optics* (Springer, 2001).
32. P. J. A. Sazio, A. Amezcua-Correa, C. E. Finlayson, J. R. Hayes, T. J. Scheidemantel, N. F. Baril, B. R. Jackson, D. J. Won, F. Zhang, and E. R. Margine, "Microstructured optical fibers as high-pressure microfluidic reactors," Science **311**, 1583–1586 (2006).
33. M. A. Schmidt, L. N. P. Sempere, H. K. Tyagi, C. G. Poulton, and P. S. J. Russell, "Waveguiding and plasmon resonances in two-dimensional photonic lattices of gold and silver nanowires," Phys Rev B **77**, 033417 (2007).
34. J. Laegsgaard, "Gap formation and guided modes in photonic bandgap fibers with high-index rods," J. Opt. A **6**, 798–804 (2004).